Research Article

Molecular Cancer Therapeutics

Effect of Pazopanib on Tumor Microenvironment and Liposome Delivery

Tina D. Tailor[1,2], Gabi Hanna[3], Pavel S. Yarmolenko[5,7], Matthew R. Dreher[7], Allison S. Betof[3,4], Andrew B. Nixon[6], Ivan Spasojevic[6], and Mark W. Dewhirst[3,4,5]

Abstract

Pathologic angiogenesis creates an abnormal microenvironment in solid tumors, characterized by elevated interstitial fluid pressure (IFP) and hypoxia. Emerging theories suggest that judicious downregulation of proangiogenic signaling pathways may transiently "normalize" the vascular bed, making it more suitable for drug delivery and radiotherapy. In this work, we investigate the role of pazopanib, a small-molecule inhibitor of vascular endothelial growth factor (VEGF) and platelet-derived growth factor (PDGF) receptors, on tumor IFP, angiogenesis, hypoxia, and liposomal drug delivery. Nude mice bearing A549 human non–small cell lung cancer xenografts were treated with 100 mg/kg pazopanib ($n = 20$) or vehicle ($n = 20$) through oral gavage for 8 days, followed by a one-time intravenous dose of 10 mg/kg Doxil (liposomal doxorubicin). Pazopanib treatment resulted in significant reduction of tumor IFP and decreased vessel density, assessed by CD31 staining. Despite these trends toward normalization, high-performance liquid chromatography revealed no differences in doxorubicin concentration between pazopanib-treated and control tumors, with Doxil penetration from microvessels being significantly reduced in the pazopanib group. Additionally, tumor hypoxia, evaluated by CA-IX immunostaining and confirmed in a second study by EF5 expression ($n = 4$, 100 mg/kg pazopanib; $n = 4$, vehicle), was increased in pazopanib-treated tumors. Our results suggest that the classic definition of tumor "normalization" may undermine the crucial role of vessel permeability and oncotic pressure gradients in liposomal drug delivery, and that functional measures of normalization, such as reduced IFP and hypoxia, may not occur in parallel temporal windows. *Mol Cancer Ther; 9(6); 1798–808. ©2010 AACR.*

Introduction

Solid tumors possess a variety of physiologic abnormalities that pose a barrier for conventional nonsurgical therapies (1). Aberrant angiogenesis drives new vessel sprouting, resulting in poorly organized vessel architecture. Tumor-associated vascular networks are haphazard and heterogeneous, exhibiting tortuous branching and arteriolar-venous shunting (2, 3). Endothelial cell tight junctions and pericytes are often absent, leading to loss of vessel integrity and leakage of plasma oncotic contents into the interstitial space. Additionally, the extracellular matrix (ECM) of tumors is reactive and contractile, supporting vascular proliferation and exerting mechanical stress on blood vessels to further compromise perfusion (2). Collectively, these characteristics create an abnormal tumor microenvironment characterized by hypoxia and elevated interstitial fluid pressure (IFP), factors thought to predispose to reduced chemosensitivity and radiosensitivity (4).

Elevations in IFP result in reduction of transvascular hydrostatic pressure gradients. This impedes the ability of systemic therapies, particularly macromolecules and liposomes, which rely on convection for transvascular transport, to traverse the endothelial barrier and penetrate the interstitium (4, 5). Studies suggest that reduction in IFP may be associated with improved delivery of chemotherapeutics and treatment response (6–8). However, also important to extravasation of liposomes is vascular permeability or endothelial pore size. By virtue of vessel hyperpermeability, liposomes and macromolecules preferentially accumulate in tumor tissue, sparing healthy tissue from excessive drug exposure (9–12).

The concept of vessel normalization was originally observed by Le Serve and Hellman, who noted that tumors treated with ICRF-159 (topoisomerase II inhibitor) exhibited more organized vessel architecture than untreated tumors, leading to the idea that these morphologic changes in vasculature may affect blood flow and drug

Authors' Affiliations: [1]Duke University School of Medicine, [2]Howard Hughes Medical Institute, Chevy Chase, Maryland; Departments of [3]Radiation Oncology, [4]Pathology, and [5]Biomedical Engineering; [6]Duke Comprehensive Cancer Care Center, Duke University Medical Center, Durham, North Carolina; and [7]Radiology and Imaging Sciences Clinical Center, NIH, Bethesda, Maryland

Corresponding Author: Mark W. Dewhirst, Department of Radiation Oncology, Duke University Medical Center, Box 3455, 201 MSRB, Research Drive, Durham, NC 27710. Phone: 919-684-4180; Fax: 919-684-8718. E-mail: dewhirst@radonc.duke.edu

doi: 10.1158/1535-7163.MCT-09-0856

delivery (3). In recent years, attention has turned to the use of antiangiogenic agents as a means to normalize the tumor microenvironment (13–18). Jain proposes that judicious attenuation of proangiogenic signaling, within in a dose- and time-dependent window period, may selectively prune immature blood vessels and remodel others. The resultant vasculature is less chaotic with greater pericyte coverage and less permeability, resembling that of normal tissue (4). These structural transformations are further thought to be accompanied by physiologic normalization parameters, such as decreased IFP and improved tumor oxygenation, factors thought to make the overall vascular network better suited for drug delivery and/or radiotherapy (4, 19). Notably, the normalization effect is transient and finite, as prolonged exposure to antiangiogenic agents creates vascular regression, which can compromise drug delivery (14, 18).

Whereas vascular endothelial growth factor (VEGF) is the principal promoter of neovascularization, small-molecule tyrosine kinase inhibitors that have a broader spectrum of activity against other angiogenic signaling molecules have shown successful clinical outcomes (20). However, few studies have investigated these agents in the context of the normalization phenomena. In this work, we investigate pazopanib, a novel second-generation multitargeted inhibitor of VEGF receptor (VEGFR)-1, VEGFR-2, and VEGFR-3; platelet-derived growth factor receptor (PDGFR)-α and PDGFR-β; and c-kit. Preclinical and clinical studies have revealed antiangiogenic and antitumor activity in various cancers, and phase II and III trials are ongoing (21–24). We examine the effect of pazopanib on tumor microenvironment in A549 human non-small cell lung cancer (NSCLC) xenografts. NSCLC exhibits elevated IFP and overexpresses PDGF, making it a suitable model for this study (8, 25). Further, the clinical treatment response to single-agent therapy is particularly poor for NSCLC, making normalization an attractive strategy to improve drug delivery or enhance other adjuvant regimens (26). We present preclinical data on the effect of pazopanib on tumor vasculature, and also provide insight into its functional effects on IFP, oxygenation, and liposomal drug delivery.

Materials and Methods

Pharmaceuticals

Pazopanib (GW786034B), benzenesulfonamide,5-[4-[(2,3-dimethyl-2*H*-indazol-6-yl)methylamino]-2-pyrimidinyl]amino]-2-methyl-monohydrochloride, was supplied by GlaxoSmithKline in powder form. Per the manufacturer's instructions, the powder was suspended in vehicle (0.5% hydroxypropylemethylcellulose, 0.1% Tween 80 in distilled water, pH adjusted to 1.3 to 1.5 with 0.1 N hydrochloric acid) to yield a concentration of 10 mg/mL. Doxil (liposomal doxorubicin, Centocor Ortho Biotech, Inc.) was purchased from the Duke Hospital pharmacy at a concentration of 2 mg/mL.

Human NSCLC xenografts

A549 cells were purchased from American Type Culture Collection. Per the cell bank, cells were verified through short-tandem repeat DNA profiling. Cells were cultured in Kaighn's F-12 medium (Invitrogen) supplemented with 10% fetal bovine serum (Invitrogen) and 1% penicillin-streptamycin (Sigma-Aldrich). Adult female nude mice were injected in the right dorsal flank with 1×10^6 cells, suspended in 1:2 (v/v) PBS/Matrigel (BD Pharmaceuticals). Animal weights and tumor volumes ($V = L \times W^2 \times \pi/6$) were measured every other day. All mice were housed in an isolated animal facility with free access to food and water. All procedures were approved and performed in accordance with the Institutional Animal Care and Use Committee guidelines.

Treatment regimen

Therapy was initiated when tumors reached a volume above 350 mm^3. Mice were randomized to receive 100 mg/kg pazopanib ($n = 20$) or vehicle control ($n = 20$), both delivered through oral gavage. Mice were treated daily for 8 days. Following the last administration of pazopanib or vehicle, all mice received a single dose of Doxil (liposomal doxorubicin) at 10 mg/kg, through intravenous tail vein injection. Animals were sacrificed with a lethal pentobarbitol dose (250 mg/kg) 24 hours after Doxil administration, in accordance with the half-life of Doxil in mice and the time of maximal tumor accumulation (12, 27). Tumors were excised, snap frozen over liquid nitrogen, and stored at −80°C.

A second smaller study ($n = 4$, control; $n = 4$, 100 mg/kg pazopanib) was carried out to confirm hypoxia trends, as assessed by the endogenous hypoxia-inducible factor-1–regulated protein CA-IX. This study was identical in design to the previous study, except that that 3 hours before sacrifice, mice received an intraperitoneal injection of 80 mg/kg EF5 [2-(2-nitro-1*H*-imidazole-1-yl)-*N*-(2,2,3,3,3-pentafluoropropyl acetamide)], a marker that binds to areas of tissue hypoxia. EF5 was generously provided by Dr. Cameron Koch (University of Pennsylvania, Philadelphia, PA).

Tumor IFP measurement

On the day of sacrifice, tumor IFP measurements were made with a needle probe pressure monitor (Intra-Compartmental Pressure Monitor System, Stryker), fitted with an 18-gauge side-ported needle (Stryker) and connected to a syringe filled with 0.9% saline.

Mice were anesthetized with isoflurane. The needle probe was inserted into the center of the tumor. IFP was recorded when the measurement stabilized. Normal muscle IFP was also measured. Tumor IFP values were normalized to muscle IFP (normalized IFP = tumor IFP/muscle IFP), and normalized IFP values were compared.

Immunohistochemistry

Half of the tumors from the first study ($n = 10$, control; $n = 9$, 100 mg/kg pazopanib) were cut into 10 μm

sections using a LEICA CM 1850 cryotome (Meyer Instruments Incorporated, Houston, TX) maintained at −24°C to −28°C. Two to three sections per tumor were stained for vasculature using anti-CD31 (cell adhesion molecule on endothelial cells). Pericyte coverage was assessed by two markers, α-smooth muscle actin (α-SMA) and NG2. Serial sections were stained with an antibody against CA-IX, an endogenous hypoxia marker. Tumors injected with EF5 were also sectioned and immunostained to detect EF5 binding. Unless otherwise stated, sections were fixed in cold methanol (stored at −20°C) for 30 minutes, followed by blocking for 30 minutes at room temperature with 10% donkey serum (Jackson Immunoresearch). Sections were incubated with primary antibodies, followed by incubation with a fluorescent-conjugated secondary antibody, where applicable. All antibodies were diluted in PBS and incubated at room temperature, unless otherwise specified. Samples were rinsed with PBS three times for 5 minutes each between every consecutive step. All staining procedures ended with a 5-minute application of Hoechst 33342 (Sigma-Aldrich) to counterstain for cellular nuclei. Stained slides were stored in 4% paraformaldehyde at 4°C. Exclusion of a primary antibody served as a negative control. Marker-specific protocols are described below.

CD31, α-SMA, and NG2. Sections were incubated for 1 hour with rat anti-mouse CD31 antibody (BD Biosciences), diluted 1:100, followed by incubation with a donkey anti-rat fluorescent secondary antibody (Alexa Fluor 488, Invitrogen), diluted 1:1,000. Pericyte coverage was assessed by α-SMA and NG2 immunostaining. Cy3-conjugated mouse monoclonal anti–α-SMA (Sigma-Aldrich) was applied at 1:400 dilution for 1 hour. For NG2 staining, slides were fixed in cold acetone at 4°C for 20 minutes instead of methanol. Slides were incubated overnight at 4°C with mouse anti-NG2 (Millipore), diluted 1:200, followed by application of a fluorescent donkey anti-mouse antibody (DyLight 459, Jackson Immunoresearch) at 1:1,000 for 1 hour. For NG2 staining, PBS with 0.2% Tween (PBST), instead of PBS, was used for washings between steps.

CA-IX. Slides were fixed in acetone for 20 minutes, dried, and blocked for 30 minutes with primary antibody dilution buffer (Biomeda). Subsequently, slides were incubated for 1 hour with rabbit polyclonal antibody to CA-IX (Abcam), diluted 1:50 in primary antibody dilution buffer. Lastly, Cy2-conjugated donkey anti-rabbit antibody (Jackson Immunoresearch), diluted 1:150, was applied for 30 minutes.

EF5. EF5 was visualized with a Cy3-conjugated mouse monoclonal ELK3-51 antibody (Jackson Immunoresearch), applied for 1 hour at 1:1,000.

Microscopy

Sections were imaged using a high-resolution solid-state camera mounted on a fluorescent microscope (Axioscop Zplus, Carl Zeiss, Inc.). Hoescht 33342 was detected using a 4′,6-diamidino-2-phenylindole filter. Doxil fluorescence and Cy3 signals were detected with a TRITC filter. CD31 staining and Cy2 signals were detected with a FITC filter.

A computer-controlled motorized stepping stage (Metamorph Imaging System, Molecular Devices Corporation) was used to automatically tile individual fields and generate up to three composite images of every tissue section. NG2 images were captured at 5× magnification. All other images were captured at 10× magnification in 16-bit monochrome signal depth. Fixed exposure times were preselected for each fluorochrome. To ensure that Doxil was not washed out during sample preparation, it was imaged first and then stained for CD31.

Image analysis

The nuclear counterstain permitted region of interest (ROI) contour lines to be drawn around each tumor, and also allowed delineation and exclusion of necrotic areas based on the absence of cellular nuclei. Mean vessel density (MVD) was determined for each section by overlaying a fixed grid over the image (Adobe Photoshop CS2) and manually counting CD31-positive structures within five random viable fields to obtain a mean value for each tumor section. Within these fields, CD31 staining was colocalized with α-SMA and NG2 staining, and the number of vessels that stained positive for these markers was determined. This latter number was divided by the total vessels in the field to determine the proportion of vessels exhibiting pericyte coverage. To quantify hypoxia, Image J (Image J, NIH, http://rsb.info.nih.gov/ij/) was used to set a single optimal threshold value for both CA-IX and EF5. The amount of positively stained area was divided by the total tumor area to obtain the area fraction of CA-IX and EF5 expression. For the purpose of presentation only, images were colored and adjusted for brightness and contrast.

Doxil penetration analysis

A previously described MATLAB algorithm was used to calculate the penetration distance of Doxil from vasculature (11, 28). Briefly, an ROI mask was defined that encompassed only the tumor and excluded artifact or necrosis. The mask was applied to CD31 and Doxil images of each slide. CD31 images were thresholded using Otsu's method to identify vessels. After the speckle noise was removed, a distance transform was done on each of the CD31 images, resulting in images whose pixel values represent distances to the nearest blood vessel. All of the tumor pixels were sorted into bins (bin width = 0.75 μm) of increasing distance from the vasculature. The average intensity of Doxil fluorescence was calculated in each distance bin. Doxil penetration was defined as the average distance at which background-adjusted average doxorubicin fluorescence decreased to 50% of its maximum value in each section. These values were obtained from interpolation of fluorescence versus distance to the nearest vascular surface in each slide. Distance to the center of each distance bin is reported.

High-performance liquid chromatography

Tumors from the first study (n = 10, control; n = 9, 100 mg/kg pazopanib) were quantified for total tumor doxorubicin concentration with high-performance liquid chromatography (HPLC). Tumors were quartered, and one fourth of each tumor was used for HPLC, as previously described (29). Briefly, samples were cryocrushed in liquid nitrogen, thawed, and homogenized. Doxorubicin was extracted using chloroform/isopropanol (4:1) and sodium tetraborate (Sigma-Aldrich). Solvents in the organic layer were removed through nitrogen stream and reconstituted in methanol, followed by centrifugation and filtration of the supernatant. Tumor doxorubicin concentration was determined with HPLC fluorescence readings of the supernatant. The HPLC readings were converted to doxorubicin concentration using a standard calibration curve that was generated using homogenized untreated tumor tissue, added to known concentrations of doxorubicin (Sigma-Aldrich).

Determination of VEGFR-2 and PDGFR-β receptor status

Tumors were homogenized and protein concentration was quantified by the Bradford method. For phosphorylated protein determination, homogenized samples (100 μg) were subjected to SDS-PAGE on 4% to 20% gradient gels (Novex Incorporated), transferred to nitrocellulose membranes, and probed using primary antibodies against phosphorylated VEGFR-2 (Santa Cruz Biotechnology) and phosphophorylated PDGFR-β (Cell Signaling Technology). Visualization was done using the appropriate fluorescently labeled secondary antibody [Alexa Fluor 680 (Invitrogen) and IRDye800 (Rockland Incorporated)] and analyzed using the Odyssey Imaging system (Li-Cor Biosciences).

Total VEGFR-2 and PDGFR-β levels were determined using the Meso Scale Discover (MSD) system. Uncoated Multi-array 96-well plates were incubated overnight with 50 μL of capture antibody to VEGFR-2 or PDGFR-β (Cell Signaling Technology) in TBS at 4°C. The antibody solution was removed and the plate was blocked with 3% blocker A/TBS for 1 hour at room temperature. Plates were washed with 0.05% Tween/TBS before addition of 50 μg tumor homogenate. Plates were incubated at room temperature for 2 hours and washed with 0.05% Tween/TBS. Biotinylated detection antibody (R&D Systems) and labeled streptavidin (SULFO-TAG, MSD) was added to each well and incubated at room temperature for 1 hour. MSD Read Buffer was added, and plates were analyzed with a SECTOR Imager 2400 (MSD) according to the manufacturer's specifications.

Statistics

Statistical analysis was carried out using JMP 8.0 (SAS Institute Incorporated). Descriptive statistics are presented as mean ± SEM. One-way ANOVA was used to compare differences in tumor volumes between groups. The paired t test was used to compare day-to-day animal weights. To avoid assumptions of a normal distribution, nonparametric tests were used for all other analyses. The Wilcoxon test was used to compare differences between groups. Spearman's rank correlation coefficient (ρ coefficient) was used to examine the relationship between two variables. $P < 0.05$ was considered statistically significant.

Results

Response to treatment

Mice were randomized to receive 100 mg/kg pazopanib (n = 20) or vehicle control (n = 20). The growth of A549 xenografts is shown in Fig. 1. Tumors treated with pazopanib had smaller volumes at study completion compared with control (720 ± 50 mm^3 control versus 570 ± 40 mm^3 pazopanib, P = 0.041). Mice experienced no significant weight changes; however, two animals receiving pazopanib died before study completion from unknown causes.

Drug distribution in pazopanib-untreated tumors

Distributions of drug with respect to vasculature and hypoxia in vehicle-treated tumors were analyzed as controls. Figure 2 (A and B) shows representative tricolor composite of control tumors, displaying Doxil (magenta) in relation to CD31-stained vasculature (green) and hypoxic regions stained with CA-IX (yellow). Images show a high concentration of Doxil around the tumor periphery, with liposomes predominantly confined to perivascular spaces. Finally, many areas of vascularity lack surrounding Doxil and also overlay hypoxic areas. Nonetheless,

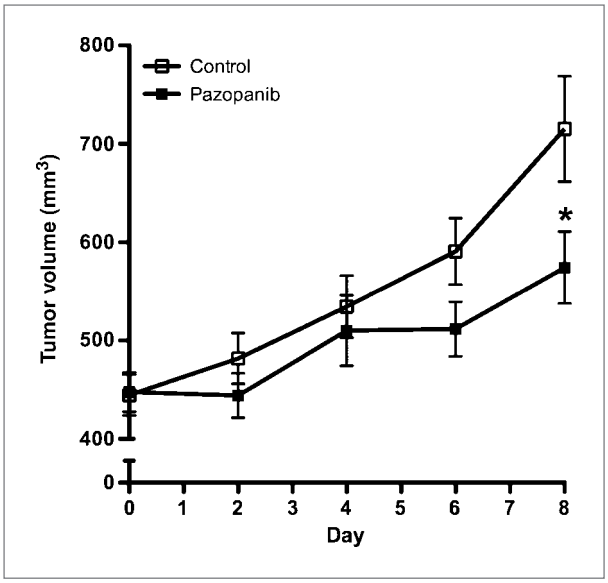

Figure 1. Tumor volume response to pazopanib. Nude mice bearing A549 human non–small cell lung cancer xenografts (>350 mm^3) were randomized to receive daily oral administration of 100 mg/kg pazopanib (n = 18) or vehicle control (n = 20), starting on day 0. Data presented as mean ± SEM. *, $P < 0.05$, one-way ANOVA.

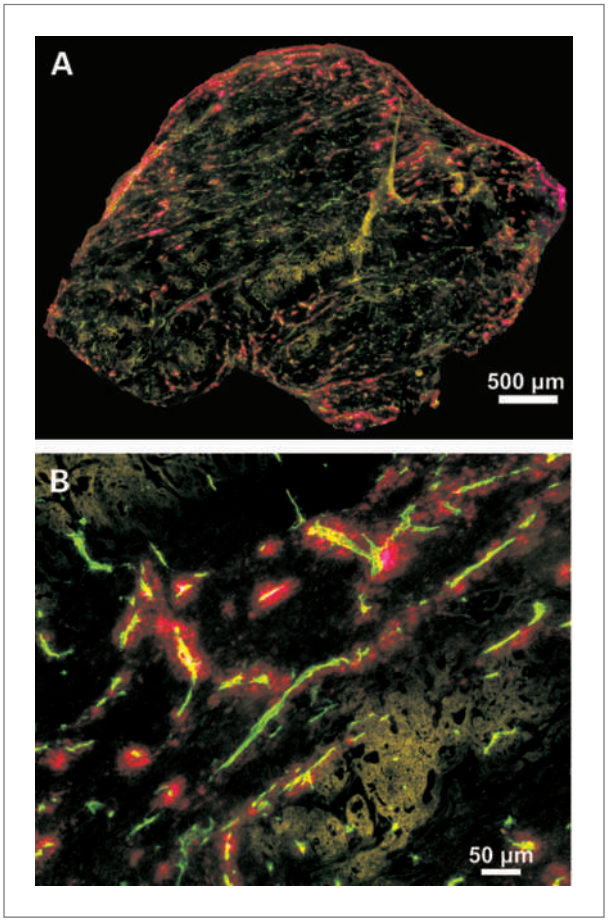

Figure 2. Representative tricolor composites of Doxil demonstrating the distribution of Doxil (magenta) in a control tumor, in relation to CD31-stained blood vessels (green) and hypoxia (CA-IX, yellow). A, whole tumor section, 10× objective. B, magnified view demonstrating perivascular accumulation of Doxil; magnification, 100%.

nuclear counterstaining with Hoescht 33342 revealed viable tissue in these areas (not shown).

Effect of pazopanib on angiogenesis

To assess the affect of pazopanib on vasculature, frozen sections were stained for CD31. Consistent with the anti-angiogenic effects of pazopanib, MVD (vessels/mm^2) was reduced in treated tumors (251 ± 19 control versus 101 ± 11 pazopanib, $P < 0.0001$; Fig. 3A and B). The proportion of pericyte-covered vessels, assessed by anti–α-SMA and anti-NG2 immunostaining, decreased in the treatment group (α-SMA: 0.84 ± 0.03 control versus 0.68 ± 0.05 pazopanib, $P = 0.016$; NG2: 0.72 ± 0.07 control versus 0.26 ± 0.04, $P < 0.001$; Fig. 3A, C–D).

IFP and hypoxia trends

Tumor IFP was measured before sacrifice, and values were normalized to normal muscle IFP. Normalized tumor IFP was decreased in the pazopanib group (14.6 ± 1.9 control versus 7.6 ± 3.2 pazopanib, $P = 0.015$; Fig. 4A). IFP was positively correlated to MVD (Spearman's $\rho = 0.7667$, $P = 0.016$; Fig. 4B).

Animals treated with pazopanib showed increased hypoxia, as quantified by CA-IX immunostaining. As shown in Fig. 4C, the percentage area staining positive for CA-IX was higher in the pazopanib-treated group (7.0 ± 1.0% control versus 16.7 ± 1.7% pazopanib, $P < 0.001$). This increase in hypoxia was confirmed by EF5 binding. Consistent with CA-IX expression, the percentage area staining positive for EF5 was higher for pazopanib-treated tumors (36.6 ± 4.6%) than control (16.0 ± 2.6%), $P = 0.007$ (Fig. 4D).

Effect of pazopanib on Doxil delivery

To assess the effect of pazopanib pretreatment on liposome delivery, mice received an intravenous injection of 10 mg/kg Doxil following an 8-day treatment course with 100 mg/kg pazopanib or vehicle control. Twenty-four hours after Doxil administration, mice were sacrificed. As shown in Fig. 5A, there was no significant difference in doxorubicin concentration between pazopanib-treated and control tumors (10.8 ± 1.8 ng/mg control versus 12.3 ± 1.0 ng/mg pazopanib, $P = 0.596$). A custom MATLAB algorithm was used to determine the fluorescence intensity of Doxil as a function of distance from the nearest microvessel. These data are presented in Fig. 5B. Doxil penetration, defined as the distance from the nearest vessel at which Doxil fluorescence dropped to 50% of its maximum, was decreased in tumors treated with pazopanib (7.7 ± 0.4 μm control versus 3.4 ± 0.7 μm pazopanib, $P = 0.024$; Fig. 5C).

Effect of pazopanib on VEGFR-2 and PDGFR-β

Phosphorylated and total levels of VEGFR-2 and PDGFR-β were determined through quantitative Western blotting and a plate-based antibody capture assay, respectively. Total receptor levels were significantly decreased in the pazopanib-treated group (VEGFR-2, $P = 0.018$; PDGFR-β, $P = 0.003$; Fig. 6A and B). Although not statistically significant, phosphorylation of PDGFR-β trended upward.

Discussion

It has been reported that tumor-associated neovascularization results in an abnormal tumor microenvironment that is unsuitable for drug delivery (4). Composite images of CD31, CA-IX, and Doxil (Fig. 2) confirm a number of unique tumor pathophysiologies. Despite an abundance of vasculature, a notable amount of tissue is hypoxic, suggesting that the vascular bed is inefficient for nutrient and oxygen transport. The reasons for these insufficiencies are multifactorial and go beyond high tissue oxygen consumption, to include vascular characteristics such as inefficient vessel architecture or vessel density, diversion from shunt flow, and inadequate intravascular partial pressure of oxygen (pO_2; ref. 30). These vessel abnormalities are reflected in the spatial distribution of

drug delivery. A dominant feature of Fig. 2 is the apparent lack of Doxil surrounding a number of blood vessels, particularly those vessels that coincide with areas of poor oxygenation. This is suggestive of regionally poor transport and functionally abnormal vasculature, and could also reflect regions of low liposome extravasation or spatial differences in vascular permeability. Consistent with previous studies, our results show that liposomes preferentially accumulate in the perivascular space (9, 31). This limited distribution is partially explained by elevated tumor IFP, which may reduce the convective fluxes that macromolecules (>10 kDa) rely on for transport into the interstitium (1, 32). The interstitial space poses yet another challenge for drug delivery, as cytokines and growth factors, notably PDGF, promote integrin-fibroblast interactions, creating stromal tension and IFP elevation (33). Such interactions also lead to a small ECM pore size and limited interconnectedness, thereby decreasing the available volume fraction for molecular transport (34). Increased solid stress from cellular proliferation may also play a role in tumor IFP elevation (35). IFP is thought to be uniformly elevated throughout the tumor mass, dropping steeply at the tumor periphery, where perfusion is also greatest (32, 36, 37). Accordingly, our results show that Doxil distribution is limited largely to the tumor periphery.

We show that modulation of VEGF and PDGF receptor signaling with pazopanib alters aspects of the tumor microenvironment in NSCLC xenografts. Elevated IFP is a hallmark of solid tumor microenvironment (5, 19). Although intravascular/extravascular compartmental pressures and transvascular fluid flux are meticulously

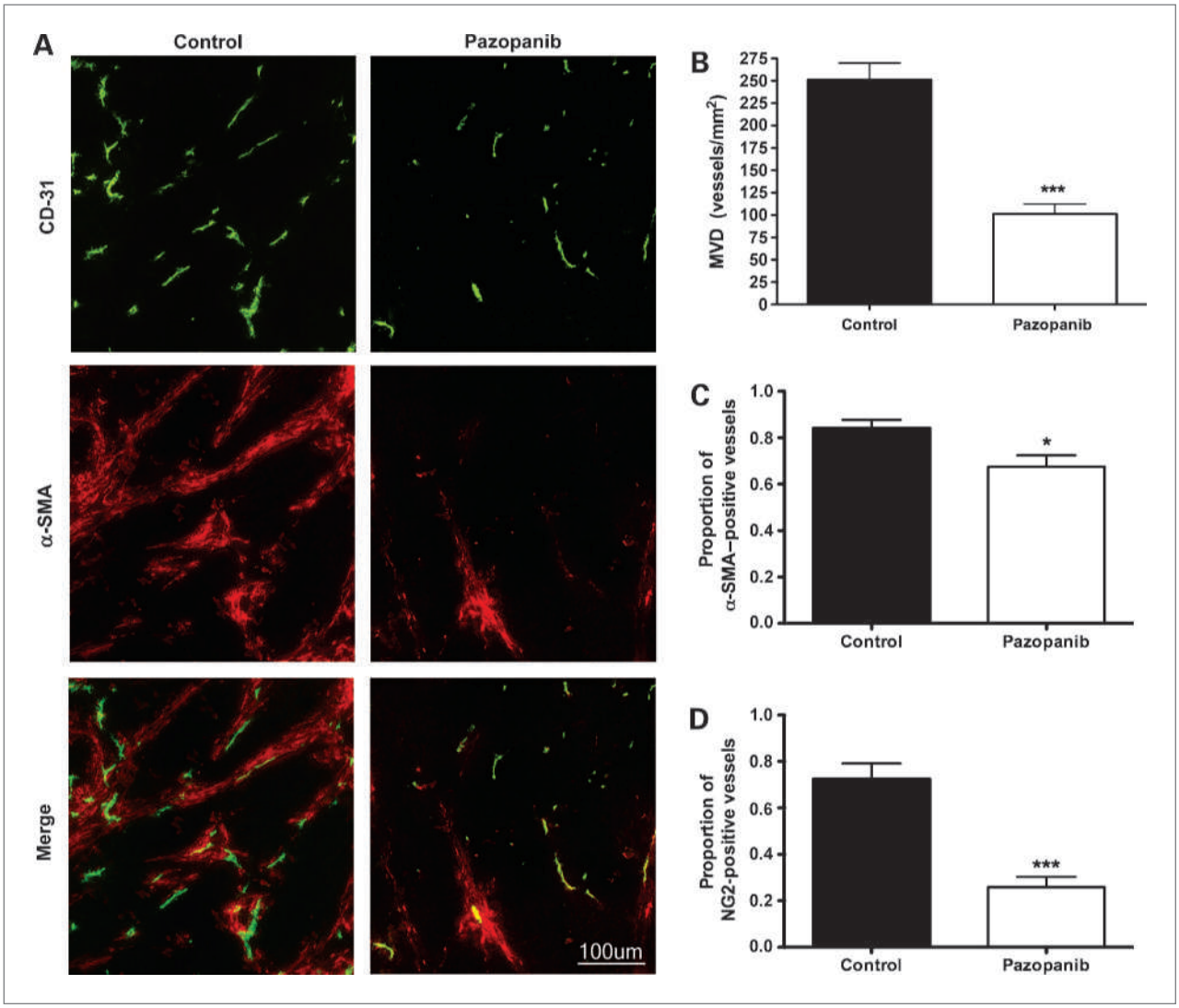

Figure 3. Effect of pazopanib on vasculature and vessel pericyte coverage. A, representative composite image of vessels (CD31, green) and pericytes (α-SMA, red). B, MVD determined by CD31 staining. C, vessel pericyte coverage determined by colocalization of CD31 and α-SMA staining. D, vessel pericyte coverage determined by colocalization of CD31 and NG2 staining. Columns, mean; bars, SEM. *, $P < 0.05$, ***, $P < 0.001$, Wilcoxon test.

maintained in normal tissues by functional lymphatics, vessel integrity, ECM interactions, and Starling forces, tumors lack such regulation (5, 32). A number of studies have noted reduction of IFP with selective inhibition of VEGFR or PDGFR (15–17, 38). However, few studies have examined the role of combination VEGFR/PDGFR blockade on tumor IFP (39, 40). Our results show that pazopanib, a tyrosine kinase receptor inhibitor of VEGR and PDGFR, causes a decrease in tumor IFP (Fig. 4A). IFP is also positively correlated with MVD (Fig. 4B), implying that vascular regression contributes to IFP reduction. VEGF is known to drive proliferation of immature, hyperpermeable blood vessels (41–43). Genetic deletion of VEGF or pharmacologic inhibition of VEGFR-2 signaling has been shown to selectively ablate immature vasculature, namely vessels that lack pericyte coverage (14, 42, 44). Our results show a significant reduction in MVD in pazopanib-treated tumors (Fig. 3A and B). We postulate that pazopanib-mediated VEGFR inhibition causes at least partial regression of leaky vasculature with overall reduction in vascular permeability. The result is reduced extravasation of plasma oncotic particles with subsequent decrease in associated transvascular fluid flux.

Pazopanib-mediated PDGFR inhibition also likely plays a role in decreasing IFP. Inhibition of this receptor not only decreases pericyte-mediated angiogenesis but downregulates the recruitment and function of fibroblasts and stromal cells (16, 32, 33, 42). As A459 also expresses PDGFR, decreased tumor cell proliferation may also be expected (35, 45). This anticellular effect, along with the stromal relaxation effects of PDGFR inhibition, may contribute to decreased solid stress and interstitial pressure.

Despite IFP reduction, tumors treated with pazopanib exhibited decreased Doxil penetration, compared with control (Fig. 5C). This is in discord with the classic normalization hypothesis that would suggest overall improved delivery. In one exemplary study of normalization, treatment with anti-VEGF reduced tumor IFP, presumably through selective pruning of leaky vasculature and decrease in vessel permeability (15). Anti-VEGF–treated tumors also exhibited deeper intratumor penetration of bovine serum albumin (BSA) molecules,

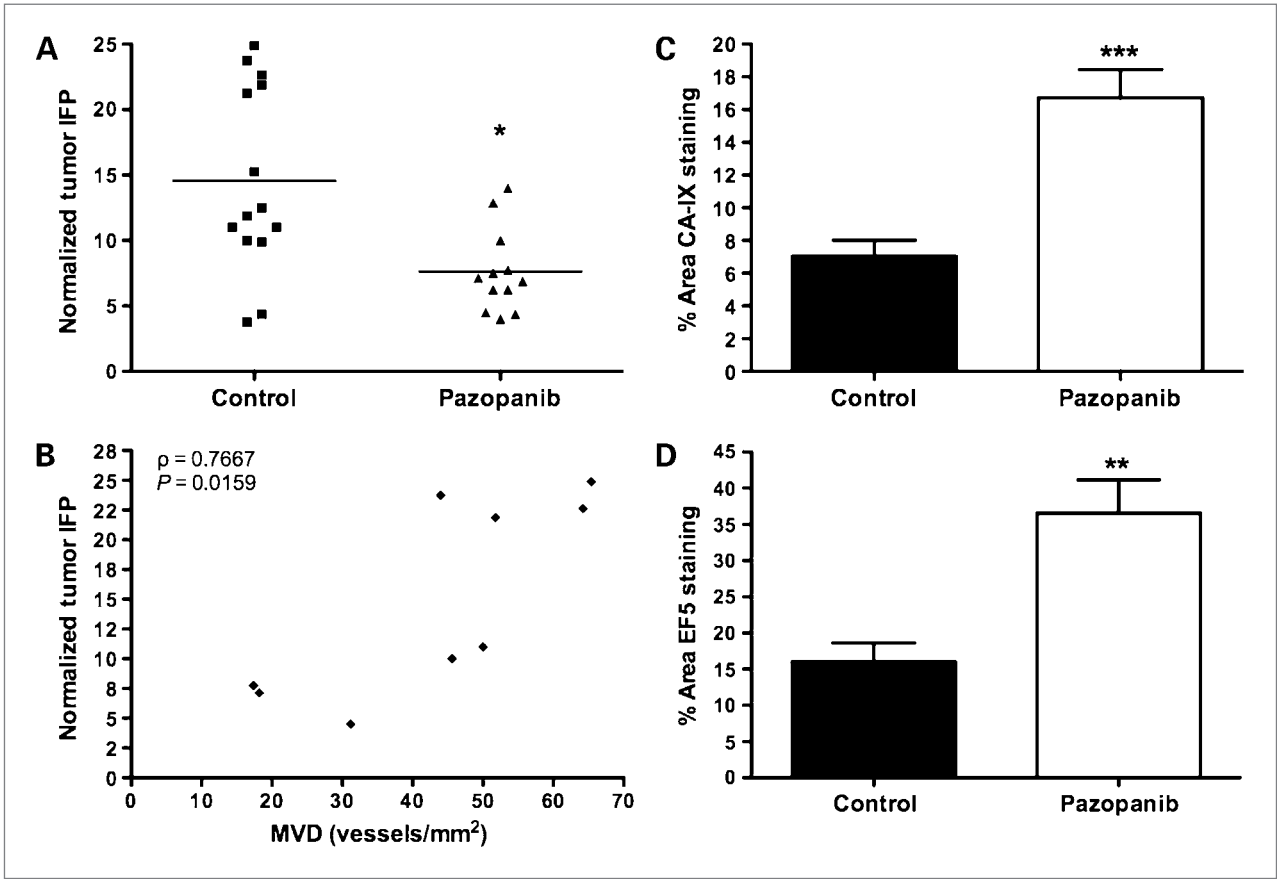

Figure 4. Comparison of IFP and hypoxia markers in pazopanib and control tumors. A, comparison of normalized tumor IFP measured at study end. Normalized tumor IFP = tumor IFP/normal muscle IFP. Horizontal bars, means. B, correlation of normalized tumor IFP versus MVD. ρ, Spearman's correlation coefficient. C, percentage of tumor section area staining positive for CA-IX. B, percentage of tumor section area staining positive for EF5. Columns, mean; bars, SEM. *, $P < 0.05$, **, $P < 0.01$, ***, $P < 0.001$, Wilcoxon test.

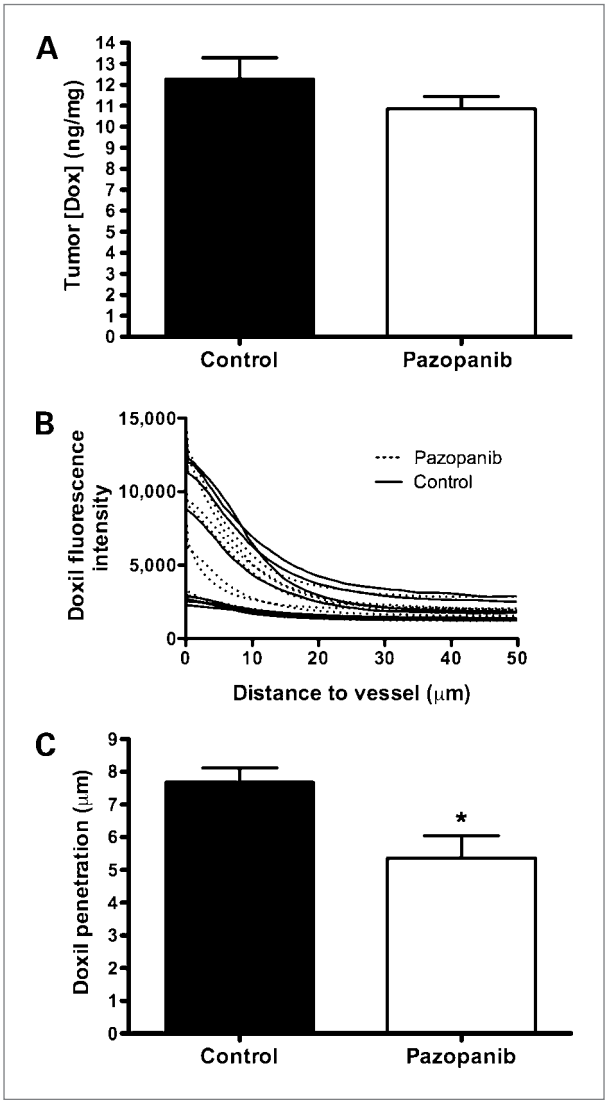

Figure 5. Effect of pazopanib on Doxil delivery. Animals were treated with 100 mg/kg pazopanib or vehicle control for 8 days, followed by a one-time dose of intravenous 10 mg/kg Doxil. A, HPLC analysis of tumor doxorubicin concentration (ng of doxorubicin/mg of tumor tissue). Columns, mean; bars, SEM. B, average fluorescence intensity of Doxil versus distance from the nearest microvessel. C, penetration distance of Doxil from CD31-stained blood vessels. Data represent the distance from the nearest microvessel at which Doxil fluorescence drops by 50% of its maximum value. *, $P < 0.05$, Wilcoxon test.

emphasizing the benefits of an induced hydrostatic pressure gradient in transvascular convection. Notably, however, BSA has a diameter of 7 nm, far smaller than liposomes (Doxil diameter ~100 nm) or tumor endothelial pores, which have been reported to be at least 400 nm (10). This size difference is important when considering that a decrease in vessel permeability may not compromise BSA transport, and in fact that a drop in vascular permeability with associated restoration of transcapillary pressures may indeed increase extravasation of molecules this size by simple virtue of favorable pressure gradients. However, simply decreasing IFP overlooks the influence of vessel permeability and oncotic pressure gradients in particle transport.

Liposomes and macromolecular drug delivery systems rely on vessel hyperpermeability for trans-endothelial transport, a phenomena coined the "enhanced permeability and retention" effect (46). By this argument and as suggested by our results, decreasing vessel permeability, as a means to normalize vasculature, may serve to hinder intratumoral delivery of liposomes. In other words, reduction of vessel leakiness may not be entirely beneficial for liposome transport, as despite favorable hydrostatic pressure gradients, particles are less able to extravasate across structurally normalized vessels with reduced permeability. Further, decreasing vessel permeability serves to increase plasma oncotic pressure, providing yet another driving force for liposomes to remain in intravascular/perivascular areas. Although we used a doxorubicin-containing liposome for this work, similar effects would be expected for any type of nanoparticle. It is important to acknowledge that Doxil penetration data were collected at a single time point in this investigation. Liposomes may continue to distribute after 24 hours; however, maximum tumor accumulation has been shown to occur at 24 hours (27).

MVD may influence the penetration of Doxil, as measured here, because a higher MVD provides more sources for Doxil to enter the tissue and penetrate the interstitium. However, our results show that the median distance from a tumor pixel to a vascular pixel is 18.8 ± 0.7 μm for the control group and 31.2 ± 1.8 μm for the pazopanib group ($P < 0.001$). As expected, the greater distance between a tumor pixel and a vascular pixel is consistent with a drop in MVD for the pazopanib group. Because these distances are much greater than the average penetration distances, it is doubtful that MVD influenced the reported penetration. Rather, the observed changes are likely dominated by permeability, convective flux, and the effective diffusion coefficient (32).

Although Doxil penetration was reduced with pazopanib pretreatment, HPLC revealed no difference in tumor doxorubicin concentration between groups (Fig. 5A). This is an intriguing observation, as MVD was decreased by >50% in pazopanib-treated tumors (Fig. 3A and C). This supports the paradigm of the tumor vascular bed being a construct of two distinct vascular networks, immature and mature (44). It is likely that the former vascular type, lacking in vessel integrity and function, is most sensitive to VEGF inhibition and therefore initially targeted by pazopanib (39, 42, 47). Hence, many lost vessels may have been completely nonfunctional and therefore had no effect on overall amount of delivery. Also plausible is that the overall reduction in intratumoral pressure may have altered blood flow in a way that positively compensated for vessel loss.

An unforeseen observation of this study was the increase in hypoxia in pazopanib-treated tumors (Fig. 4C and D). Preliminary work done in this xenograft

suggested improved oxygenation after 8 days of treatment with 100 mg/kg pazopanib (data not shown), providing justification for the dosing and duration of drug used in this study. However, our data are suggestive of excessive vessel regression with this treatment course. This trend of vascular regression is supported by increased expression of hypoxia markers, CA-IX and EF5, as well as histologic analysis of pericytes stained with anti–α-SMA and NG2. As shown in Fig. 3C and D, the proportion of pericyte-coated vessels decreases with pazopanib administration. This is in accordance with pazopanib antagonism of PDGFRs. PDGFR signaling is imperative for angiogenesis, as it triggers recruitment of fibroblasts and perivascular cells. These mural cells secrete cytokines to support vessel proliferation, and also provide structural and hemostatic control of nascent vessel sprouts to bring about vessel maturity (48). PDGF inhibition has been shown to decrease periendothelial cells, a trend that digresses from the structural features of vessel normalization (8, 47). Despite these effects, previous studies report decreased IFP, improved oxygenation, and enhanced cytotoxic drug delivery with PDGF inhibitors such as imatinib and sunitinib (8, 16, 38, 39). This suggests that downregulation of PDGF signaling may contribute to functional vessel normalization, partially through blockade of pericyte-mediated angiogenesis. However, continuous exposure to pazopanib and other vessel-disrupting agents likely destroys pericyte-endothelial cell interactions, ultimately compromising mature tumor vasculature and causing hypoxia (13, 39).

The finding of increased hypoxia reiterates the precise sensitivity of drug dosing and timing that is required for normalization to occur. Jain proposes a "normalization window," wherein IFP is reduced and tumor oxygenation is improved. However, our results show that the fluctuations in these functional measures of normalization may not parallel one another. Whereas IFP may remain decreased for several days following the initiation of anti-VEGF therapy, improvements in oxygenation may be short-lived, as little as 1 day in some cases (13, 15, 18). Therefore, in contrast to previous studies that have used IFP as a primary marker of normalization, our data imply that the window of normalization may be better assessed by oxygenation status (4, 15, 39). This is reiterated by Cao et al., who show that systemic overexpression of angiopoietin-2 (endothelial Tie-2 receptor agonist) causes significant vessel dropout with improved perfusion in the remaining vessels (49). Despite the increase in perfusion, hypoxia was exacerbated, highlighting the delicate interplay between parameters such as vessel density and structure, blood flow, perfusion, and oxygenation. The dynamic nature of these parameters, along with the varying effects of dosing, timing, and type of vessel-targeting therapy, must be accounted for when considering normalization.

Also important, although largely overlooked by the normalization hypothesis, is the spatial and temporal heterogeneity of perfusion and hypoxia, as well as downstream signaling pathways that are activated by changes in hypoxia (30). Pertinent to this discussion, hypoxia may induce phosphorylation of PDGFR-β and induce cell survival through a hypoxia-inducible factor-1α–mediated pathway (50). Our results show a decrease in total levels of VEGFR-2 and PDGFR-β with pazopanib, consistent

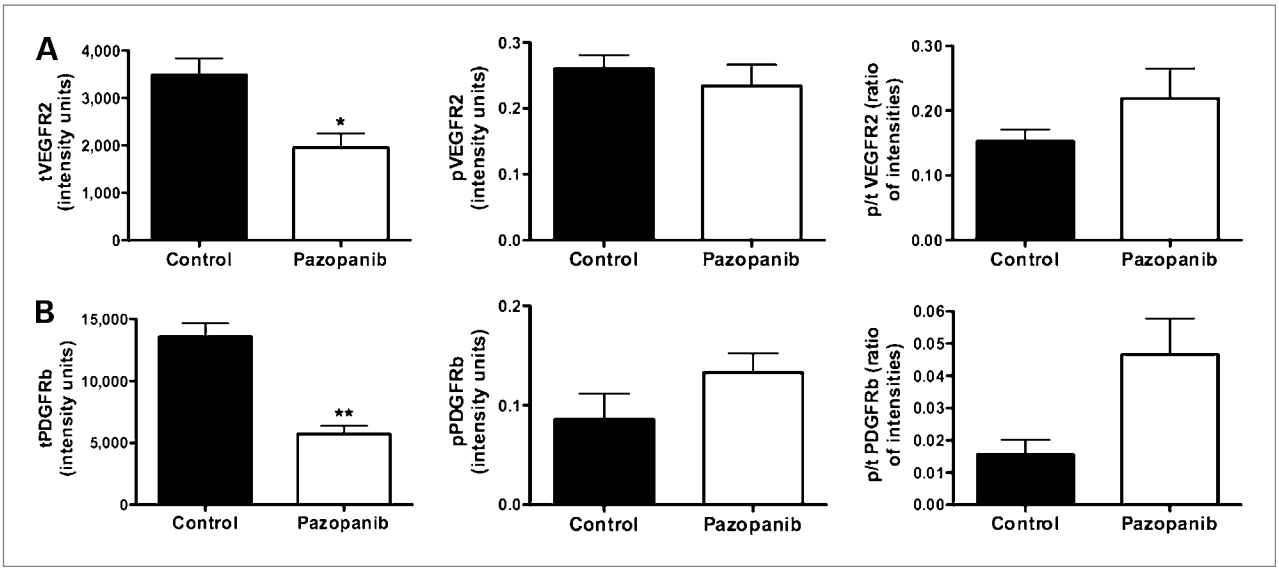

Figure 6. Total and phosphorylated levels of VEGFR-2 and PDGFR-β. A plate-based antibody capture assay (Meso Scale Discovery platform) was used to quantify total receptor levels in vehicle-treated control tumors and pazopanib-treated tumors. Phosphorylated receptor levels were determined through quantitative Western blotting. A, relative intensity values for total and phosphorylated VEGFR-2, and "activation status," expressed as the ratio of phosphorylated/total VEGFR-2. B, relative intensity values for total PDGFR-β, phosphorylated PDGFR-β, and activation status. Columns, mean; bars, SEM. *, $P < 0.05$, **, $P < 0.01$, Wilcoxon test.

with a decrease in endothelial cells and pericytes and/or stromal cells, respectively, as well as overall tumor volume (Fig. 1). Although phosphorylated levels of both receptor types were statistically unchanged, phosphorylation of PDGFR-β seemingly trended upward, perhaps suggesting hypoxic receptor activation that may compete with the mechanism of action of pazopanib.

In conclusion, this investigation shows that pazopanib exerts antivascular effects in NSCLC xenografts and that concurrent VEGFR/PDGFR inhibition may be a useful approach to modulate and normalize the tumor microenvironment. VEGFR and PDGFR inhibition likely decrease IFP through at least two distinct mechanisms. The former causes a regression of dysfunctional, leaky vessels, with an associated decrease in interstitial colloid osmotic pressure, whereas anti-PDGFR activity likely hampers ECM interactions to loosen an otherwise stiff stroma. Although the observed trends in IFP support the normalization hypothesis, the reduced penetration of liposomes in pazopanib-treated tumors suggests that the normalization phenomenon undermines the enhanced permeability and retention effect that is fundamental to liposome transport. Decreasing vessel permeability to restore transcapillary pressure gradients may be of questionable benefit for liposome extravasation. Finally, the finding of increased hypoxia and decreased pericyte coverage, suggesting destruction of mature vessels in pazopanib-treated tumors, underscores the seemingly transient nature of the normalization window. Although this investigation is limited by a single time point and antiangiogenic agents have temporal effects on vasculature that are not studied here, the question of feasibility, particularly in the clinical setting, for achieving the precision in dosing and timing of drug delivery required for structural vessel normalization, while still remaining in a window that normalizes functional parameters like IFP and oxygenation, is debatable. Nonetheless, as more multitargeted antiangiogenic agents emerge into clinical use, it will be of crucial importance to understand their dynamic role on tumor structure and function to achieve optimal anticancer effect.

Disclosure of Potential Conflicts of Interest

M. Dewhirst: grant support, GlaxoSmithKline. No other potential conflicts of interest were disclosed.

Acknowledgments

We thank Joseph Herbert for his assistance with animal work.

Grant Support

Research contract from GlaxoSmithKline and support from Duke Cancer Center and Howard Hughes Medical Institute.

The costs of publication of this article were defrayed in part by the payment of page charges. This article must therefore be hereby marked *advertisement* in accordance with 18 U.S.C. Section 1734 solely to indicate this fact.

Received 09/18/2009; revised 04/09/2010; accepted 04/16/2010; published OnlineFirst 06/01/2010.

References

1. Jain RK. Barriers to drug delivery in solid tumors. Sci Am 1994;271:58–65.
2. Cairns R, Papandreou I, Denko N. Overcoming physiologic barriers to cancer treatment by molecularly targeting the tumor microenvironment. Mol Cancer Res 2006;4:61–70.
3. Le Serve AW, Hellmann K. Metastases and the normalization of tumour blood vessels by ICRF 159: a new type of drug action. Br Med J 1972;1:597–601.
4. Jain RK. Normalization of tumor vasculature: an emerging concept in antiangiogenic therapy. Science 2005;307:58–62.
5. Heldin CH, Rubin K, Pietras K, Ostman A. High interstitial fluid pressure—an obstacle in cancer therapy. Nat Rev Cancer 2004;4:806–13.
6. Pietras K, Rubin K, Sjoblom T, et al. Inhibition of PDGF receptor signaling in tumor stroma enhances antitumor effect of chemotherapy. Cancer Res 2002;62:5476–84.
7. Salnikov AV, Iversen VV, Koisti M, et al. Lowering of tumor interstitial fluid pressure specifically augments efficacy of chemotherapy. FASEB J 2003;17:1756–8.
8. Vlahovic G, Ponce AM, Rabbani Z, et al. Treatment with imatinib improves drug delivery and efficacy in NSCLC xenografts. Br J Cancer 2007;97:735–40.
9. Yuan F, Leunig M, Huang SK, Berk DA, Papahadjopoulos D, Jain RK. Microvascular permeability and interstitial penetration of sterically stabilized (stealth) liposomes in a human tumor xenograft. Cancer Res 1994;54:3352–6.
10. Yuan F, Dellian M, Fukumura D, et al. Vascular permeability in a human tumor xenograft: molecular size dependence and cutoff size. Cancer Res 1995;55:3752–6.
11. Dreher MR, Liu W, Michelich CR, Dewhirst MW, Yuan F, Chilkoti A. Tumor vascular permeability, accumulation, and penetration of macromolecular drug carriers. J Natl Cancer Inst 2006;98:335–44.
12. Gabizon A, Shmeeda H, Barenholz Y. Pharmacokinetics of pegylated liposomal doxorubicin: review of animal and human studies. Clin Pharmacokinet 2003;42:419–36.
13. Ansiaux R, Baudelet C, Jordan BF, et al. Mechanism of reoxygenation after antiangiogenic therapy using SU5416 and its importance for guiding combined antitumor therapy. Cancer Res 2006;66:9698–704.
14. Dickson PV, Hamner JB, Sims TL, et al. Bevacizumab-induced transient remodeling of the vasculature in neuroblastoma xenografts results in improved delivery and efficacy of systemically administered chemotherapy. Clin Cancer Res 2007;13:3942–50.
15. Tong RT, Boucher Y, Kozin SV, Winkler F, Hicklin DJ, Jain RK. Vascular normalization by vascular endothelial growth factor receptor 2 blockade induces a pressure gradient across the vasculature and improves drug penetration in tumors. Cancer Res 2004;64:3731–6.
16. Vlahovic G, Rabbani ZN, Herndon JE II, Dewhirst MW, Vujaskovic Z. Treatment with Imatinib in NSCLC is associated with decrease of phosphorylated PDGFR-β and VEGF expression, decrease in interstitial fluid pressure and improvement of oxygenation. Br J Cancer 2006;95:1013–9.
17. Willett CG, Boucher Y, di Tomaso E, et al. Direct evidence that the VEGF-specific antibody bevacizumab has antivascular effects in human rectal cancer. Nat Med 2004;10:145–7.
18. Winkler F, Kozin SV, Tong RT, et al. Kinetics of vascular normalization by VEGFR2 blockade governs brain tumor response to radiation:

role of oxygenation, angiopoietin-1, and matrix metalloproteinases. Cancer Cell 2004;6:553–63.
19. Fukumura D, Jain RK. Tumor microvasculature and microenvironment: targets for anti-angiogenesis and normalization. Microvasc Res 2007;74:72–84.
20. Marx J. Cancer. Encouraging results for second-generation antiangiogenesis drugs. Science 2005;308:1248–9.
21. Hurwitz HI, Dowlati A, Saini S, et al. Phase I trial of pazopanib in patients with advanced cancer. Clin Cancer Res 2009;15:4220–7.
22. Kumar R, Knick VB, Rudolph SK, et al. Pharmacokinetic-pharmacodynamic correlation from mouse to human with pazopanib, a multikinase angiogenesis inhibitor with potent antitumor and antiangiogenic activity. Mol Cancer Ther 2007;6:2012–21.
23. Podar K, Tonon G, Sattler M, et al. The small-molecule VEGF receptor inhibitor pazopanib (GW786034B) targets both tumor and endothelial cells in multiple myeloma. Proc Natl Acad Sci U S A 2006;103:19478–83.
24. Sleijfer S, Ray-Coquard I, Papai Z, et al. Pazopanib, a multikinase angiogenesis inhibitor, in patients with relapsed or refractory advanced soft tissue sarcoma: a phase II study from the European organisation for research and treatment of cancer-soft tissue and bone sarcoma group (EORTC study 62043). J Clin Oncol 2009;27:3126–32.
25. Sause W, Kolesar P, Taylor SI, et al. Final results of phase III trial in regionally advanced unresectable non-small cell lung cancer: Radiation Therapy Oncology Group, Eastern Cooperative Oncology Group, and Southwest Oncology Group. Chest 2000;117:358–64.
26. Lilenbaum RC, Herndon JE II, List MA, et al. Single-agent versus combination chemotherapy in advanced non-small-cell lung cancer: the cancer and leukemia group B (study 9730). J Clin Oncol 2005;23:190–6.
27. Charrois GJ, Allen TM. Rate of biodistribution of STEALTH liposomes to tumor and skin: influence of liposome diameter and implications for toxicity and therapeutic activity. Biochim Biophys Acta 2003;1609:102–8.
28. Moeller BJ, Dreher MR, Rabbani ZN, et al. Pleiotropic effects of HIF-1 blockade on tumor radiosensitivity. Cancer Cell 2005;8:99–110.
29. Palmer GM, Boruta RJ, Viglianti BL, Lan L, Spasojevic I, Dewhirst MW. Non-invasive monitoring of intra-tumor drug concentration and therapeutic response using optical spectroscopy. J Control Release 2010;142:457–64.
30. Dewhirst MW, Cao Y, Moeller B. Cycling hypoxia and free radicals regulate angiogenesis and radiotherapy response. Nat Rev Cancer 2008;8:425–37.
31. Kong G, Braun RD, Dewhirst MW. Hyperthermia enables tumor-specific nanoparticle delivery: effect of particle size. Cancer Res 2000;60:4440–5.
32. Bouzin C, Feron O. Targeting tumor stroma and exploiting mature tumor vasculature to improve anti-cancer drug delivery. Drug Resist Updat 2007;10:109–20.
33. Ostman A. PDGF receptors-mediators of autocrine tumor growth and regulators of tumor vasculature and stroma. Cytokine Growth Factor Rev 2004;15:275–86.
34. Yuan F, Krol A, Tong S. Available space and extracellular transport of macromolecules: effects of pore size and connectedness. Ann Biomed Eng 2001;29:1150–8.
35. Sarntinoranont M, Rooney F, Ferrari M. Interstitial stress and fluid pressure within a growing tumor. Ann Biomed Eng 2003;31:327–35.
36. Jain RK, Tong RT, Munn LL. Effect of vascular normalization by antiangiogenic therapy on interstitial hypertension, peritumor edema, and lymphatic metastasis: insights from a mathematical model. Cancer Res 2007;67:2729–35.
37. Viglianti BL, Abraham SA, Michelich CR, et al. *In vivo* monitoring of tissue pharmacokinetics of liposome/drug using MRI: illustration of targeted delivery. Magn Reson Med 2004;51:1153–62.
38. Pietras K, Ostman A, Sjoquist M, et al. Inhibition of platelet-derived growth factor receptors reduces interstitial hypertension and increases transcapillary transport in tumors. Cancer Res 2001;61:2929–34.
39. Zhou Q, Guo P, Gallo JM. Impact of angiogenesis inhibition by sunitinib on tumor distribution of temozolomide. Clin Cancer Res 2008;14:1540–9.
40. Klosowska-Wardega A, Hasumi Y, Burmakin M, et al. Combined antiangiogenic therapy targeting PDGF and VEGF receptors lowers the interstitial fluid pressure in a murine experimental carcinoma. PLoS One 2009;4:e8149.
41. Dvorak HF, Brown LF, Detmar M, Dvorak AM. Vascular permeability factor/vascular endothelial growth factor, microvascular hyperpermeability, and angiogenesis. Am J Pathol 1995;146:1029–39.
42. Greenberg JI, Shields DJ, Barillas SG, et al. A role for VEGF as a negative regulator of pericyte function and vessel maturation. Nature 2008;456:809–13.
43. Rapisarda A, Melillo G. Role of the hypoxic tumor microenvironment in the resistance to anti-angiogenic therapies. Drug Resist Updat 2009;12:74–80.
44. Benjamin LE, Golijanin D, Itin A, Pode D, Keshet E. Selective ablation of immature blood vessels in established human tumors follows vascular endothelial growth factor withdrawal. J Clin Invest 1999;103:159–65.
45. Reinmuth N, Liersch R, Raedel M, et al. Combined anti-PDGFRα and PDGFRβ targeting in non-small cell lung cancer. Int J Cancer 2009;124:1535–44.
46. Maeda H, Wu J, Sawa T, Matsumura Y, Hori K. Tumor vascular permeability and the EPR effect in macromolecular therapeutics: a review. J Control Release 2000;65:271–84.
47. Bergers G, Song S, Meyer-Morse N, Bergsland E, Hanahan D. Benefits of targeting both pericytes and endothelial cells in the tumor vasculature with kinase inhibitors. J Clin Invest 2003;111:1287–95.
48. Carmeliet P. Mechanisms of angiogenesis and arteriogenesis. Nat Med 2000;6:389–95.
49. Cao Y, Sonveaux P, Liu S, et al. Systemic overexpression of angiopoietin-2 promotes tumor microvessel regression and inhibits angiogenesis and tumor growth. Cancer Res 2007;67:3835–44.
50. Zhang SX, Gozal D, Sachleben LR, Jr., Rane M, Klein JB, Gozal E. Hypoxia induces an autocrine-paracrine survival pathway via platelet-derived growth factor (PDGF)-B/PDGF-β receptor/phosphatidylinositol 3-kinase/Akt signaling in RN46A neuronal cells. FASEB J 2003;17:1709–11.